AIAA
P 90-2340

AIAA

AIAA-90-2340

A90-42777

Methods for Determining the Internal Thrust of Scramjet Engine Modules from Experimental Data

Randall T. Voland
NASA Langley Research Center
Hampton, VA

AIAA/SAE/ASME/ASEE
26th Joint Propulsion Conference
July 16-18, 1990/Orlando, FL

For permission to copy or republish, contact the American Institute of Aeronautics and Astronautics
370 L'Enfant Promenade, S.W., Washington, D.C. 20024

METHODS FOR DETERMINING THE INTERNAL THRUST OF SCRAMJET ENGINE MODULES FROM EXPERIMENTAL DATA

P90-U2777

by
Randall T. Voland*
NASA Langley Research Center
Hampton, Virginia

AIAA/SAE/ASME/ASEE 26th Joint Propulsion Conference
July 16-18, 1990
Orlando, Florida

ABSTRACT

The major thrust performance parameter (ΔF) for subscale scramjet engine module ground tests is the measured difference in axial force on the module with fuel injection and without fuel injection. This parameter, however, only accounts for changes in forces in the combustor and nozzle of the engine module. To accurately predict the performance of a full-scale integrated engine/airframe system from data generated in subscale ground tests of single scramjet engine modules, the internal thrust of the subscale module tested must be calculated. The internal thrust accounts for all internal forces on the module including the zero-fuel internal drag. The internal thrust is only a function of the ΔF and the zero-fuel internal drag. The ΔF is measured directly during engine tests, so the focus of this paper is to develop methods to determine the zero-fuel internal drag from engine test data. Three methods to determine zero-fuel internal drag of a sidewall compression scramjet engine module, with inlet spillage, are developed. The methods used are an integration of surface pressures and skin friction, and momentum balances on two different control volumes. These three techniques are then applied to zero-fuel test data from a version of the NASA Langley Research Center parametric scramjet.

NOMENCLATURE

A_c	cowl area, inlet geometric projected area
A_s	surface area
A_x	projection of surface area in axial direction
A_1	captured streamtube area
A_3	engine module exit streamtube area
C_F	local skin friction coefficient
$C_{\tau,\phi=0}$	zero-fuel internal drag coefficient
CV1	control volume 1, see figure 9a
CV2	control volume 2, see figure 9b
D_a	inlet additive drag
D_p	plume drag
D_s	drag on portion of inlet internal sidewall not washed by captured flow
F	force
$F_{spill,out}$	axial component of momentum of flow spilled from inlet
$F_{\tau,\phi}$	internal thrust
$F_{\tau,\phi=0}$	zero-fuel internal drag
$H_{t,\infty}$	freestream total enthalpy
M	local Mach number
M_1	inlet entrance Mach number
M_∞	freestream Mach number
P	static pressure
$P_{t,1}$	total pressure at inlet entrance
Re_x	local Reynolds number based on length
q	dynamic pressure
T	static temperature
T_w	wall temperature
$T_{t,1}$	total temperature at inlet entrance
u	axial velocity component
ϕ	fuel equivalence ratio
ρ	density

*Aerospace Engineer, Hypersonic Propulsion Branch, Member AIAA

Copyright © 1990 by the American Institute of Aeronautics and Astronautics, Inc. No copyright is asserted in the United States under Title 17, U.S. Code. The U.S. Government has a royalty-free license to exercise all rights under the copyright claimed herein for Governmental purposes. All other rights are reserved by the copyright owner.

ΔF	change from zero-fuel to fuel on engine module axial force
μ	viscosity

INTRODUCTION

Since the late 1950's, NASA and other government agencies have been working toward the goal of sustained hypersonic flight within the atmosphere. The scramjet engine (supersonic combustion ramjet) has emerged from this research as the leading propulsion system candidate for this type vehicle. A vehicle using scramjet engines is more efficient than one using rockets for sustained hypersonic flight because it captures the oxygen required for combustion directly from the atmosphere rather than carrying the oxygen on board. However, for the scramjet to yield sufficient net thrust for flight, installation drag must be minimized by integrating the scramjet modules with the vehicle. In general, this integration consists of installing a cluster of identical engine modules on the undersurface of the vehicle such that the forebody of the vehicle performs some of the required airflow compression for the engine inlet, and the aftbody of the aircraft serves as a nozzle expansion surface as shown in figure 1a.

The methods used to simulate flight conditions during ground tests of subscale airframe-integrated scramjet modules are illustrated in figure 1b. These ground test techniques and their associated limitations are discussed in references 1 and 2. In ground tests a single subscale engine module is mounted on an axial force measurement system in a wind-tunnel which is capable of producing hypersonic flow at true flight enthalpy. In flight, the engines are mounted on the vehicle forebody such that they are inside the envelope of the bow shock. Thus, at the engine inlet face, the flow has a total enthalpy equal to the freestream total enthalpy, $H_{t,\infty}$, but a Mach number, M_1, less than the freestream Mach number, M_∞. Therefore, in ground tests, the test gas is heated to a total enthalpy corresponding to some flight Mach number and altitude, but the flow is expanded in the facility nozzle to a lower Mach number representative of the Mach number behind the bow shock of some vehicle. The engine is generally mounted in the tunnel so that it ingests the facility nozzle boundary layer which simulates some of the effects of vehicle forebody boundary layer ingestion in flight.

The ultimate goal of propulsion tests in ground facilities is to demonstrate that the engines will provide adequate performance in flight. To determine this, certain key parameters must be measured in the ground tests. A major performance parameter is ΔF, i.e., the axial force component of the engine with fuel injection at some flight condition, minus the axial force on the engine with no fuel injection at the same flight condition. Thus, if the external flow over the engine module and the internal flow in the inlet do not change between the unfueled and fueled cases, ΔF is the change in internal axial force on the combustor and nozzle of the engine due to combustion. The ΔF is, therefore, a very important, and easily measured, parameter in engine tests. However, when accounting for scramjet engine forces on an aircraft, or for comparing the performance of different engine designs, ΔF is an insufficient performance parameter.

References 3-7 describe the test results of a variety of scramjet engine designs. Scramjet engine designs vary widely as is illustrated in figure 2, especially the inlet and nozzle designs, and thus the drag characteristics of these scramjets would be different. It is less obvious from figure 2, but the details of the combustor design (flameholders, etc.) can also significantly affect drag. Since ΔF only accounts for the change in axial force on the combustor and nozzle of the engine due to fuel injection, and not the initial combustor, nozzle, or inlet drag; it is more suited for comparing the effects of small design changes to combustor or nozzle geometry within a single engine design class than for performance comparisons between different types of scramjet engines.

To accurately compare the performance of different scramjet engine designs, it is necessary to calculate the performance of the integrated engine/airframe system. References 7-11 discuss the calculation of installed performance for a variety of scramjet engines on a number of different vehicles. Most of these reports describe purely analytical methods of determining installed performance and thus do not make use of any test data. Anderson (ref. 7) and Pinckney (ref. 8) do, however, use some test data to account for certain engine forces.

The present research was undertaken to expand on the work of Anderson and Pinckney by demonstrating methods of determining one particular engine force, zero-fuel internal drag, $F_{\tau,\phi=0}$, utilizing engine test data from the NASA Langley Research Center parametric scramjet engine, rather than depending entirely on analytical modeling of the engine flowfield. Zero-fuel internal drag is vital in the projection of engine test data to flight on a vehicle, because when combined with ΔF it determines the internal thrust, $F_{\tau,\phi}$, of the engine. The internal thrust of an engine module includes all of the forces on the internal flow path, and thus can be used directly, along with the aerodynamic characteristics of a vehicle, to determine the flight performance of the integrated engine/airframe system.

The purpose of this paper is to introduce the methodology used to calculate internal thrust from measurements of ΔF and calculations of zero-fuel internal drag, and develop and demonstrate the methods of calculating zero-fuel internal drag from engine test data. The zero-fuel internal drag can be calculated from either engine surface measurement integrations or a momentum balance on a control volume drawn around the engine. The surface measurement integration technique can in theory be applied to any engine design, but the control volume approach requires some alterations depending on the type of engine being analyzed and the data available. Two control volumes were developed for calculating the zero-fuel internal drag through sidewall compression engine modules with inlet spillage. All three zero-fuel internal drag calculation techniques are applied to test data from a version of the NASA Langley Research Center parametric scramjet, which is of the sidewall compression class. Although some simplifying assumptions were made in this analysis, due to a lack of data in certain areas, the validity of the calculation methods is demonstrated.

THEORY

Internal thrust in the axial direction at any fuel equivalence ratio, $F_{\tau,\phi}$, is a function of only the ΔF and the zero-fuel internal drag $F_{\tau,\phi=0}$:

$$F_{\tau,\phi} = \Delta F + F_{\tau,\phi=0} \tag{1}$$

This relationship is developed in reference 4. The sign convention used throughout this paper is that a positive force (i.e., thrust) acts on the engine module opposite to the flow direction. The ΔF is measured during scramjet engine tests, while the zero-fuel internal drag must be calculated.

Zero-fuel internal drag is the combination of all the forces on the internal surfaces of the scramjet with no fuel flow. These forces are a combination of both pressure and skin friction forces. There are two methods to calculate zero-fuel internal drag from experimental measurements. The first is to integrate the axial component of pressure force over the internal surfaces using the measured wall static pressures and then add the integrated skin friction force. The second method is to use a control volume approach to compute the momentum change through the engine, which if properly applied, equals the surface force integral.

The application of either the pressure and skin friction integral or the control volume method to calculate zero-fuel internal drag is relatively straightforward for simple engine geometries, but as the scramjet geometry becomes more complex, care must be taken in their application. The wall pressure/skin friction integral technique can, in principle, always be used no matter how complex the configuration, however, the engine module must be sufficiently instrumented to obtain an accurate calculation of this integral. This degree of instrumentation is very difficult to obtain in practice, and hence, the control volume technique may prove to be the only practical way of calculating the zero-fuel internal drag to determine the internal thrust of complex scramjet engine modules.

Figure 3a illustrates the integration of sidewall compression scramjet engines on an aircraft. The airflow streamtube captured by the inlet and processed through the engine is illustrated by the dashed lines on the figure. This type of engine may not capture all the flow approaching it as illustrated in figure 3b. Of the flow passing through the cowl area, A_C, only that portion which also passes through the capture area, A_I, is captured by the inlet. The remainder of the airflow enters the inlet but spills through its open bottom. The calculation of zero-fuel internal drag using a pressure and skin friction integral is

straightforward for this type of engine, as long as the internal geometry is not too complex; however, the flow spillage through the bottom of the inlet introduces some difficulties in computing the zero-fuel internal drag using a control volume.

Figure 3b outlines one control volume which could be used to determine the zero fuel internal drag. This control volume would include only the captured streamtube starting at A_1 and ending at station 3. The change in the momentum through the control volume is equal to the sum of the forces on the control surfaces (ref. 12). This control volume, however, contains streamtube surfaces which are not physical surfaces. The axial force computed from the momentum change of the captured streamtube from 1 to 3 will include pressure area forces even on the streamtube surfaces which are not physical surfaces. These pressure forces are only a concern on the non-physical surfaces which are not parallel to the flow direction, because they contribute a fictitious thrust or drag increment in the axial direction. To determine the axial force on only the physical surfaces of the control volume, the pressure forces on these non-parallel, non-physical streamtube surfaces must be cancelled by an equal and opposite force. In the control volume of figure 3b, two of these streamtube surfaces exist. The first is at the bottom of the inlet where the streamtube curves due to the flow turning from the swept-shock compression process, and the second is between the engine cowl exit and station 3 where the streamtube curves to match pressure and flow direction with the free stream. The integral of the pressure times the axial projected area along these two curved streamtubes must be added to the momentum balance to cancel the fictitious contributions to the internal drag due to these surfaces. These two cancelling forces are referred to as additive drag, D_a, for the curved streamtube in the inlet, and plume drag, D_p, for the curved streamtube at the cowl exit (ref. 13 and 14). One more term must be accounted for in this control volume to calculate zero-fuel internal drag. This term is due to the drag on the internal inlet surface which is outside of the captured streamtube, as illustrated by the crosshatched region in figure 3b. The forces on this surface are measured by the force balance, and therefore must be accounted for or an error will result when applying equation 1. This term will be called the sidewall drag, D_s. The equation for the zero-fuel internal drag using the control volume of figure 3b is then:

$$F_{\tau,\phi=0} = \sum_1^3 PA_x + \sum_1^3 C_F q A_s$$
$$= \left(\rho_3 u_3^2 + P_3\right) A_3 - \left(\rho_1 u_1^2 + P_1\right) A_1 + D_a + D_p + D_s \quad (2)$$

Two methods can be used to account for this sidewall force, D_s. The first would be to integrate the pressure and skin friction forces on it, which in most cases should be relatively easy due to the simple geometry (planar walls) of the region. The main difficulty with this method is defining the geometry of the captured streamtube so that an accurate surface force integration can be made. A method which alleviates the problem of defining this streamtube, at the expense of introducing new difficulties, would be to redefine the control volume as indicated in figure 4. The previous control volume only allowed mass to cross its boundaries at the inflow station and the outflow station, the other boundaries were either streamtube surfaces or physical surfaces and thus did not allow mass to cross. By defining the control volume so that all internal engine surfaces are within it, the axial component of the momentum crossing the lower boundary must be known. Thus, the inlet additive drag terms in equation 2 would be redefined as an axial spillage momentum term, $F_{spill,out}$. The zero-fuel internal drag for this control volume is defined by:

$$F_{\tau,\phi=0} = \left[\left(\rho_3 u_3^2 + P_3\right) A_3 + F_{spill,out}\right] - \left(\rho_1 u_1^2 + P_1\right) A_c + D_p \quad (3)$$

EXPERIMENTAL METHOD

The experimental portion of this investigation was conducted in the NASA Langley Research Center Arc-Heated Scramjet Test Facility (AHSTF). An elevation view of the tunnel circuit is shown in figure 5. The AHSTF is designed to test subscale, boilerplate, hydrogen-burning scramjet engines at true flight enthalpies from Mach 4.7 to 8 at a variety of altitudes. It can also be operated at less than true flight enthalpy during tests without combustion in the engine, as

was done in the present set of tests. The facility and its operation are described in detail in references 15, 16, and 17.

A version of the NASA Langley Parametric Scramjet engine, which is of the sidewall compression class and is described in reference 18, was the engine module used in the present study. The parametric engine is a durable set of hardware which can be quickly and easily reconfigured such that parametric variations in engine flow path can be investigated. The hardware consists of flat plates for the top surface and cowl of the engine, and segmented sidewalls. All of the flow path geometric variations are obtained by moving these sidewall segments relative to each other or by replacing whole segments.

The particular engine configuration used in these experiments is shown in figure 6. It consists of a sidewall compression inlet with 30-degree swept leading edges and 10-degree compression surfaces, a short constant-area section, and three diverging combustor sections. In the set of tests analyzed in this paper, the engine was mounted such that it ingested the boundary layer on the top wall of the Mach 6 facility nozzle in an attempt to investigate the effect of boundary layer ingestion on engine performance. The nozzle exit boundary layers, bulk flow parameters, and distributions of flow parameters for this facility have been previously characterized by both flowfield surveys and CFD in work reported in references 16 and 17. The results of the flow field surveys will be used in the present analysis.

The instrumentation used in the present tests consisted of 127 wall static pressures distributed along the engine internal and external surfaces. Instream static pressure, pitot pressure, and total temperature measurements were taken at the exit of the engine. The probes used were all of standard design and are shown in figure 7. The instream measurements were used to determine the exit momentum of the engine and thus a high density of measurements had to be taken to define all the internal losses. Figure 8 shows the locations where the instream measurements were taken. Since the engine was mounted to ingest the upper nozzle wall boundary layer, the top portion of the engine contained a large region of low energy air and thus extra measurements were taken in this region.

ANALYSIS

Three methods were used to determine zero-fuel internal drag. The first two were momentum balances on the flow entering and exiting the engine, but using different control volumes. The third was a pressure and skin friction integration over the internal surfaces of the engine. The internal surfaces of the engine will be defined, for the purposes of this paper, as the top plate and cowl plate exposed to the internal flow from their leading edges to the end of the sidewalls (station 57.575, figure 6), and the entire internal surface of the sidewalls, including the internal surfaces of the inlet not washed by the captured flow.

Figure 9 shows the two control volumes used in the momentum balance analysis. The first control volume, CV1, starts at the facility nozzle exit plane, and continues through the inlet, bounded on three sides by the top plate and the sidewalls, and on the bottom side by the last captured streamlines. The control volume ends at the exit plane of the sidewalls. The second control volume, CV2, also starts at the facility nozzle exit plane, but includes the entire inlet, not just the portions of the inlet washed by the captured flow. CV2 also ends at the exit plane of the sidewalls. The differences in analyzing the two control volumes are that CV1 only has inflow and outflow at the entrance and exit, respectively, where CV2 also has outflow along the bottom boundary of the inlet. Equation 2 will be used to analyze CV1, and equation 3 will be used for CV2. In both cases $D_p = 0$ since the control volume ends at the end of the sidewalls.

The exit momentum term for both control volumes was determined from the measurements of static pressure, pitot pressure, and total temperature made at the sidewall exit plane. The experimental measurements were interpolated to the same 11 x 11 grid by linear interpolation assuming symmetry about the vertical centerline. The data were taken over a number of runs, and run-to-run variations were corrected to the reference stagnation conditions of 394 psia and 2690° R. The interpolated and corrected data sets are presented in tables 1-3. Perfect gas relations were used to calculate the momentum flux terms at each location in the grid, and then these terms were multiplied by the appropriate area and summed to obtain the total momentum term. The local momentum terms are presented in table 4.

The entrance momentum was calculated in a similar fashion using the data from reference 16 corrected to the stagnation conditions of 394 psia and 2690° R. For CV2, the entrance momentum terms were summed over the entire projected area of the inlet. To determine the entrance momentum of CV1, the location and shape of the captured streamtube had to be determined.

The captured streamtube shape and location was estimated by using the inviscid, 2-D, swept shock inlet program of reference 19 to calculate the flow properties in each of the inlet shock bays. The calculated static pressures were higher than the measured pressures, as shown in figure 10, because the calculation assumes an infinite swept wedge, while the actual inlet flow is influenced by end effects. The captured streamtube shape and location was found by incrementally expanding the inlet flow in each shock bay by a given amount and compressing the external flow by the same amount until a pressure and flow direction match between the internal and external flow was found for each bay. Individual streamlines were then traced backwards from the cowl lip to the inlet face using the appropriate flow direction in each shock bay crossed. These individual streamlines form the bottom surface of the captured streamtube shown in figure 11. With the captured streamtube surface defined, the entrance unit momentum terms were integrated over the capture area to get the total entrance momentum.

Figure 10 also shows the calculated pressure distribution with spillage. The average measured pressures fall between the computed results for 2-D and 2-D modified for spillage effects indicating the influence of end effects on the flow. In addition to the spillage causing lower pressures near the bottom of the inlet, the swept-shock compression process causes the flow to turn away from the inlet top surface leading to a lowered pressure near the top. Thus the highest pressures tend to occur near mid-height in the inlet. This trend was seen in the sidewall pressure distributions, but there were not enough pressure taps near the bottom of the streamtube to get an absolute comparison with the calculations.

To determine the internal drag using CV1, the additive drag and the drag on the internal surfaces outside of the captured streamtube must be determined. The additive drag was found by multiplying the pressure along the bottom surface of the captured streamtube for each bay by the forward facing area over which it acted. The drag on the internal inlet surfaces outside of the captured flow area was determined by using the last captured streamline against the sidewall to define the sidewall area outside of that washed by the captured flow, and then integrating the pressure and skin friction forces over this area. The pressures used in this integration were those calculated on the bottom surface of the captured streamtube. Measured wall pressures would have been used if there had been enough of them in the area of interest. The skin friction was calculated using Spalding and Chi (ref. 20), and will be discussed further below.

The analysis of CV2 required the definition of the axial component of the flow spilling through the bottom of the inlet. There were no measurements made at the bottom plane of the inlet from which to anchor calculations of the momentum across this boundary; thus, the momentum across this boundary had to be calculated. The results of the 2-D inlet flow calculation along with the measured mass flows in and out of the engine were used to calculate the axial component of the spilled momentum. The area weighted average axial velocity of the spilled flow was calculated from the velocity vectors and areas of each shock bay in the inlet. This average axial velocity was then multiplied by the spilled mass flow to obtain the axial component of the spilled momentum, $F_{spill,out}$.

The pressure integration was accomplished by defining a forward or rearward facing area around each of the wall static pressure taps on the internal surface of the engine, then multiplying this pressure by the appropriate area. The skin friction calculation was done using both Spalding and Chi and Van Dreist II, references 20 and 21. To use either of these methods, the distribution of flow properties throughout the engine had to be known. The inflow and outflow conditions were well defined by the instream measurements, however, the only measurements taken during these tests inside the engine flow path were wall static pressures. To determine the other required parameters, the results of the swept shock inlet code were again employed. Since the overall average-measured static pressure distribution through the inlet was somewhat less than that

calculated, the calculated static pressures through the inlet were lowered to be more in line with the measured values, and then assuming the same losses as originally calculated, corrected static temperature and Mach number distributions were determined. Beyond the inlet throat an isentropic expansion was assumed. With these corrected distributions of static pressure, temperature and Mach number, all the required parameters for the calculation of skin friction were determined. These calculated parameter distributions are listed in table 5.

RESULTS AND DISCUSSION

Since the analysis of CV1 depends on the accurate determination of the captured streamtube shape and location, an independent check was made on its accuracy. The mass flow exiting the engine was calculated from the integration of the exit stream measurements, and compared to the mass flow entering the engine integrated over the captured streamtube area. These two mass flows were within 2.6 percent. Since these mass flows were so close, it was assumed that the captured streamtube was well defined.

The forces acting on control volumes CV1 and CV2 are shown in figures 12 and 13. All forces are shown with the sign resulting from the use of equations 2 and 3, where drag is negative and thrust is positive. Using equation 2 with CV1 and equation 3 with CV2, zero-fuel internal drags of -35.60 and -33.45 were calculated, respectively. The pressure integration over the internal surfaces of the engine resulted in a drag force of -7.23 lbf, and the skin friction integration gave -26.70 lbf of drag for the Spalding and Chi method, and -24.07 lbf for Van Dreist II. Combining the skin friction and pressure integrations, zero-fuel drags of -33.93 lbf or -31.30 lbf result depending on the skin friction calculation used.

Table 6 summarizes the results of all the calculations of zero fuel internal drag. Although a number of assumptions and simplifications were used in this demonstration of the zero-fuel internal drag calculation methods, all of the methods agree within 7 percent of the mean. It should be noted that the value of zero-fuel internal drag calculated using the control volumes is on the order of 10 percent of the value of the incoming momentum. This is a relatively small portion of the total momentum, but the close agreement of the momentum balance methods with the pressure/skin friction integration method tends to increase confidence in the control volume methods. These demonstration calculations also point out a number of areas where improvements in the measurements taken could enhance confidence in the final results. In the analysis of CV1, additional wall static pressure taps in the inlet along the area of the interface between the captured and spilled flows would help in both the definition of the captured streamtube, and the force on the wall outside of the captured streamtube. Instream measurements in the inlet to directly measure the captured streamtube would probably disturb the flow too much to be of use, but a full 3-D Navier-Stokes CFD solution of the inlet flow would be useful in determining the shape, location, and forces on the captured streamtube if a high enough density of grid points were used. The analysis of CV2 would also benefit from a CFD solution, or perhaps some instream measurements of the external flow just below the inlet to help determine the momentum of the spilled flow. Finally, the skin friction calculation could be improved by the addition of heat transfer measurements, or skin friction gages.

The zero-fuel internal drag calculations were performed using results obtained in a flow at Mach 6 with stagnation conditions of 394 psia and 2690° R. These stagnation conditions were chosen to increase the survivability of the probes used in the instream measurements; however, during engine tests including combustion, the flow stagnation conditions would be raised to approximately 4000° R and a pressure ranging from 300 psia to 550 psia at a Mach 6 inlet entrance condition depending on the flight dynamic pressure simulation desired. Since combustion tests occur over a range of dynamic pressures, the zero-fuel internal drag should be put into a coefficient form based on inlet entrance dynamic pressure and cowl area, A_c. Using the mean calculated zero-fuel internal drag, $F_{\tau,\phi=0}$ = -33.57 lbf, with an A_c of 42.26 square inches and an inlet entrance dynamic pressure of 765 psf; the zero-fuel internal drag coefficient, $C_{\tau,\phi=0}$ = 0.150.

CONCLUDING REMARKS

Methods to calculate zero-fuel internal drag of scramjet engine modules from experimental

measurements were developed. These methods included two control volume approaches, and a pressure and skin friction integration. The three calculation techniques were applied to experimental data taken during tests of a version of the NASA Langley Research Center parametric scramjet. The methods agreed to within 7 percent of the mean value of zero-fuel internal drag even though several simplifying assumptions were made in the analysis. The mean zero-fuel internal drag coefficient for this particular engine, based on cowl area, A_C, and inlet entrance dynamic pressure, was calculated to be 0.150. The zero-fuel internal drag coefficient when combined with ΔF (i.e., the change in engine axial force with and without fuel) defines the internal thrust of an engine which is important in making projections of subscale engine performance to full scale flight performance.

ACKNOWLEDGEMENT

This research represents a portion of the work being done by the author to complete a Master of Science degree at George Washington University. The complete work will be presented in a thesis at a later date.

REFERENCES

1. Thomas, Scott R.; and Guy, R. Wayne: Scramjet Testing From Mach 4 to 20, Present Capability and Needs for the Nineties. AIAA Paper 90-1388, presented at the AIAA 16th Aerodynamic Ground Testing Conference, June 1990.

2. Thomas, S. R.; Guy, R. W.; Voland, R. T.; and Andrews, E. H., Jr.: Subscale Scramjet Test Techniques at NASA Langley. NASP Paper No. 113, Fourth National Aerospaceplane Symposium, February 1988. (Confidential)

3. Jilly, L. F., Editor: Hypesonic Research Engine Project—Phase II, Aerothermodynamic Integration Model Development, Final Technical Report. NASA Contract No. NAS1-6666, Document No. AP-75-11133.

4. Burnette, T. D.: Dual Mode Scramjet—Part III, Engine Design and Performance Characteristics. The Marquardt Corporation, Technical Report AFAPL-TR-67-132, Part III, June 1968.

5. Guy, R. W.; Pinckney, S. Z.; and Andrews, E. H., Jr.: Summary of NASA Langley's Scramjet Engine Tests. JANNAF Propulsion Meeting, April 1985. (Confidential)

6. Guy, R. W.; Thomas, S. R.; and Voland, R. T.: Scramjet Database Development. NASP Paper Number 46A, Fourth National Aerospaceplane Technology Symposium, February 1988. (Confidential)

7. Anderson, Griffin Y.; and Mackley, Ernest A.: Mach 7 Performance of the Langley Airframe-Integrated Modular Scramjet. 1983 JANNAF Propulsion Meeting, vol. V, CPIA Pub. 370, Feb. 1983, pp. 493-508. (Confidential)

8. Pinckney, S. Z.: Internal Performance Predictions for Langley Scramjet Engine Module. NASA TMX-74038, January 1978.

9. Sullins, G. A.; and Billig, F. S.: Force Accounting for Airframe Integrated Engines. AIAA-87-1965, AIAA/SAE/ASME/ASEE 23rd Joint Propulsion Conference, June 1987.

10. Stevens, M. J.: Thrust Drag Accounting. JANNAF 1979 Propulsion Meeting, vol. V, pp. 309-339. (Confidential)

11. Waltrip, P. J.; Billig, F. S.; and Stockbridge, R. D.: Engine Sizing and Integration Requirements for Hypersonic Airbreathing Missile Applications. NATO/AGARD/PEP 58th Symposium.

12. Liepmann, H. W.; and Roshko, A.: Elements of Gasdynamics. John Wiley and Sons, 1957.

13. Ferri, Antonio; and Nucci, Louis M.: Preliminary Investigation of a New Type of Supersonic Inlet. NACA Report 1104, 1952.

14. Sibulkin, Merwin: Theoretical and Experimental Investigation of Additive Drag. NACA Report 1187, 1954.

15. Thomas, S. R.; and Guy, R. W.; Expanded Operational Capabilities of the Langley

Mach 7 Scramjet Test Facility. NASA TP 2186, 1983.

16. Thomas, S. R.; Voland, R. T.; and Guy, R. W.: Test Flow Calibration Study of the Langley Arc-Heated Scramjet Test Facility. AIAA-87-2165, AIAA/SAE/ASME/ASEE 23rd Joint Propulsion Conference, June 1987.

17. Ostrander, M. J.; Thomas, S. R.; Voland, R. T.; Guy, R. W.; and Srinivasan, S.: CFD Simulation of Square Cross-Section, Contoured Nozzle Flows: Comparison with Data. AIAA Paper 89-0045, January 1989.

18. Voland, R. T.; Thomas, S. R.; and Guy, R. W.: Thrust Performance of a Strutless Parametric Scramjet at Simulated Flight Mach Numbers of 4.7 through 8. 1987 JANNAF Propulsion Meeting, December 1987. (Confidential)

19. Trexler, C. A.; and Souders, S. W.: Design and Performance at a Local Mach Number of 6 of an Inlet for an Integrated Scramjet Concept. NASA TN D-7944, August 1975.

20. Spalding, D. B.; and Chi, S. W.: The Drag of a Compressible Turbulent Boundary Layer on a Smooth Flat Plate With and Without Heat Transfer. J. of Fluid Mechanics, vol. 18, p. 117, 1964.

21. Cebeci, T.; and Bradshaw, P.: Physical and Computational Aspects of Convective Heat Transfer. Springer-Verlag, New York, 1984, p. 343.

$P_{t,exit}$ (psia) $P_{t,1}$ = 394 psia $T_{t,1}$ = 2690° R

Height z(in.)	Width, y(in.) -2.935	-2.5	-2.0	-1.5	-1.0	-0.5	0	0.5	1.0	1.5	2.0	2.5	2.935
0.0	.300	.321	.343	.340	.337	.335	.333	.335	.337	.340	.342	.321	.300
0.1375	.305	1.761	1.972	2.183	2.394	2.770	3.146	2.770	2.394	2.183	1.972	1.761	.305
0.40	.310	2.500	2.770	3.175	3.848	4.015	4.391	4.015	3.848	3.175	2.770	2.500	.310
0.60	.315	2.755	3.231	4.079	4.483	5.051	4.872	5.051	4.483	4.079	3.231	2.755	.315
1.35	.325	3.449	4.142	4.392	5.106	5.412	5.772	5.412	5.106	4.392	4.142	3.449	.325
2.10	.330	4.143	5.107	5.800	6.138	6.417	6.673	6.417	6.138	5.800	5.107	4.143	.330
2.85	.315	4.446	6.368	7.292	9.134	9.749	9.639	9.749	9.134	7.292	6.368	4.446	.315
3.60	.285	6.308	9.687	11.369	11.252	11.159	10.814	11.159	11.252	11.369	9.687	6.308	.285
4.35	.270	4.139	7.813	10.143	10.881	12.250	12.211	12.250	10.881	10.143	7.813	4.139	.270
5.10	.250	3.546	6.667	7.390	7.909	9.236	8.505	9.236	7.909	7.390	6.667	3.546	.250
5.85	.223	3.334	4.866	6.418	7.911	8.706	8.178	8.706	7.911	6.418	4.866	3.334	.223
6.60	.195	3.087	5.166	5.999	7.509	8.320	7.807	8.320	7.509	5.999	5.166	3.087	.195
7.20	.175	.183	.191	.197	.203	.209	.216	.209	.203	.197	.191	.183	.175

Table 1. Engine Exit Pitot Pressures

P_{exit} (psia) $P_{t,1}$ = 394 psia $T_{t,1}$ = 2690° R

Height z(in.)	Width, y(in.) -2.935	-2.5	-2.0	-1.5	-1.0	-0.5	0	0.5	1.0	1.5	2.0	2.5	2.935
0.0	.300	.321	.343	.340	.337	.335	.333	.335	.337	.340	.342	.321	.300
0.1375	.305	.320	.338	.330	.327	.325	.223	.325	.327	.330	.338	.320	.305
0.40	.310	.320	.332	.321	.318	.316	.314	.316	.318	.321	.332	.320	.310
0.60	.315	.320	.326	.312	.309	.307	.305	.307	.309	.312	.326	.320	.315
1.35	.325	.321	.318	.308	.305	.303	.305	.303	.305	.308	.318	.321	.325
2.10	.330	.313	.296	.302	.305	.308	.319	.308	.305	.302	.296	.313	.330
2.85	.315	.308	.301	.317	.333	.350	.355	.350	.333	.317	.301	.308	.315
3.60	.285	.294	.304	.349	.347	.345	.359	.345	.347	.349	.304	.294	.285
4.35	.270	.289	.308	.334	.339	.345	.363	.345	.339	.334	.308	.289	.270
5.10	.250	.245	.240	.224	.236	.248	.227	.248	.236	.224	.240	.245	.250
5.85	.223	.214	.206	.205	.225	.245	.221	.245	.225	.205	.206	.214	.223
6.60	.195	.200	.206	.210	.216	.225	.217	.225	.216	.210	.206	.200	.195
7.20	.175	.183	.191	.197	.203	.209	.216	.209	.203	.197	.191	.183	.175

Table 2. Engine Exit Static Pressures

$T_{t,exit}$ (°R) $P_{t,1}$ = 394 psia $T_{t,1}$ = 2690° R

Height z(in.)	Width, y(in.) -2.935	-2.5	-2.0	-1.5	-1.0	-0.5	0	0.5	1.0	1.5	2.0	2.5	2.935
0.0	800	800	800	800	800	800	800	800	800	800	800	800	800
0.1375	800	1110	1215	1232	1278	1273	1267	1273	1278	1232	1215	1110	800
0.40	800	1418	1565	1662	1757	1746	1735	1746	1757	1662	1565	1418	800
0.60	800	1726	1948	2092	2236	2219	2202	2219	2236	2092	1948	1726	800
1.35	800	1927	2058	2076	2247	2205	2163	2205	2247	2076	2058	1927	800
2.10	800	2108	2203	2195	2351	2332	2313	2332	2351	2195	2203	2108	800
2.85	800	2234	2313	2276	2517	2522	2528	2522	2517	2276	2313	2234	800
3.60	800	2429	2519	2522	2607	2610	2613	2610	2607	2522	2519	2429	800
4.35	800	2045	2416	2485	2585	2587	2589	2587	2585	2485	2416	2045	800
5.10	800	1974	2362	2427	2553	2558	2564	2558	2553	2427	2362	1974	800
5.85	800	1847	2282	2409	2537	2549	2561	2549	2537	2409	2282	1847	800
6.60	800	1869	2335	2433	2532	2545	2558	2545	2532	2433	2335	1869	800
7.20	800	800	800	800	800	800	800	800	800	800	800	800	800

Table 3. Engine Exit Total Temperatures

$(\rho u^2 A + pA)_{exit}$ (lbf) $P_{t,1} = 394$ $psia$ $T_{t,1} = 2690°$ R

Height z(in.)	-2.935	-2.5	-2.0	-1.5	-1.0	-0.5	0	0.5	1.0	1.5	2.0	2.5	2.935
							Width, y(in.)						
0.0	0.0	0.0	0.0	0.0	0.0	0.0	0.0	0.0	0.0	0.0	0.0	0.0	0.0
0.1375	0.0	.379	.309	.340	.370	.425	.474	.425	.370	.340	.309	.379	0.0
0.40	0.0	.453	.366	.416	.500	.521	.568	.526	.500	.416	.366	.453	0.0
0.60	0.0	1.022	.870	1.087	1.191	1.338	1.291	1.338	1.191	1.087	.870	1.022	0.0
1.35	0.0	1.829	1.744	1.844	2.134	2.258	2.405	2.258	2.134	1.844	1.744	1.829	0.0
2.10	0.0	2.180	2.133	2.416	2.555	2.668	2.774	2.668	2.555	2.416	2.133	2.180	0.0
2.85	0.0	2.333	2.648	3.027	3.779	4.033	3.989	4.033	3.779	3.027	2.648	2.333	0.0
3.60	0.0	3.279	3.999	4.692	4.644	4.606	4.467	4.606	4.644	4.692	3.999	3.279	0.0
4.35	0.0	2.173	3.236	4.189	4.492	5.049	5.037	5.049	4.492	4.189	3.236	2.173	0.0
5.10	0.0	1.861	2.758	3.049	3.262	3.805	3.503	3.805	3.262	3.049	2.758	1.861	0.0
5.85	0.0	1.746	2.018	2.650	3.261	3.588	3.369	3.588	3.261	2.650	2.018	1.746	0.0
6.60	0.0	2.303	2.783	3.224	4.025	4.456	4.183	4.456	4.025	3.224	2.783	2.303	0.0
7.20	0.0	0.0	0.0	0.0	0.0	0.0	0.0	0.0	0.0	0.0	0.0	0.0	0.0

Table 4. Engine Exit Momentum

												Spalding and Chi	Van Driest II	
x (in)	A_s (in^2)	P (psia)	T (°R)	M	u (ft/s)	ρ (lbm/ft^3)	q (psi)	μ ($lbf \cdot s/ft^2$)	Re_x	$\frac{T_w}{T}$	C_F	F (lbf)	C_F VDII	F (lbf)
4	26.04	0.69	473	4.84	5159	.0039	11.20	3.48×10^{-7}	5.99×10^5	1.48	.0020	0.58	.0019	.55
8	62.90	0.69	473	4.84	5159	.0039	11.20	3.48×10^{-7}	1.20×10^6	1.48	.0018	1.27	.0017	1.20
12	67.19	0.69	473	4.84	5159	.0039	11.20	3.48×10^{-7}	1.80×10^6	1.48	.0016	1.20	.0016	1.20
16	65.26	2.96	759	3.57	4821	.0096	24.08	4.96×10^{-7}	3.90×10^6	0.92	.0018	2.83	.0017	2.67
20	66.16	2.96	759	3.57	4821	.0096	24.08	4.96×10^{-7}	4.9×10^6	0.92	.0018	2.87	.0016	2.55
24	66.16	2.96	759	3.57	4821	.0096	24.08	4.96×10^{-7}	5.9×10^6	0.92	.0017	2.70	.0016	2.55
28	67.84	2.81	656	3.96	4971	.0116	30.94	4.46×10^{-7}	9.4×10^6	1.07	.0015	3.15	.0014	2.94
32	71.20	1.93	589	4.26	5067	.0088	24.39	4.12×10^{-7}	9.0×10^6	1.19	.0015	2.60	.0013	2.26
36	74.56	1.44	541	4.51	5142	.0072	20.55	3.86×10^{-7}	8.9×10^6	1.29	.0015	2.30	.0013	1.99
40	78.88	1.00	488	4.82	5219	.0055	16.17	3.56×10^{-7}	8.4×10^6	1.43	.0014	1.79	.0012	1.53
44	84.16	0.75	449	5.08	5276	.0045	13.52	3.33×10^{-7}	8.1×10^6	1.56	.0013	1.48	.0011	1.25
48	89.44	0.59	419	5.30	5318	.0038	11.60	3.15×10^{-7}	8.0×10^6	1.67	.0012	1.25	.0011	1.14
52	94.72	0.48	395	5.49	5348	.0033	10.19	3.00×10^{-7}	7.9×10^6	1.77	.0012	1.16	.0010	0.97
56	100.00	0.40	375	5.67	5382	.0029	9.07	2.87×10^{-7}	7.9×10^6	1.87	.0012	1.09	.0010	0.91
57.575	40.82	0.38	369	5.73	539	.0028	8.80	2.83×10^{-7}	8.0×10^6	1.90	.0012	0.43	.0010	0.36
										Total	Force	26.70		24.07

Table 5. Skin Friction Calculation Parameters

Method	$F_{\tau,\phi=0}$ (lbf)	% of Mean
CV1	-35.60	6.1%
CV2	-33.45	-0.4 %
Pressure and Skin Friction Integration		
a) Spalding and Chi	-33.93	1.1%
b) Van Driest	-31.30	-6.8%
	Mean = -33.57	

Table 6. Zero-Fuel Internal Drag Summary

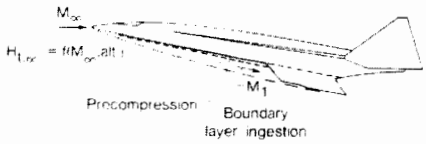

(a) Flight.

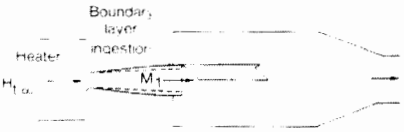

(b) Simulation in ground facility.

Figure 1.- Simulation of flight conditions.

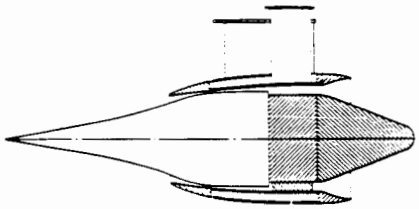

(a) NASA hypersonic research engine.

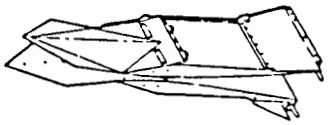

(b) Marquardt dual mode scramjet.

(c) NASA Langley three-strut engine.

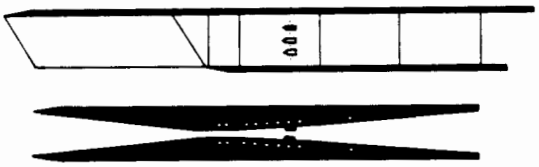

(d) NASA Langley strutless parametric engine.

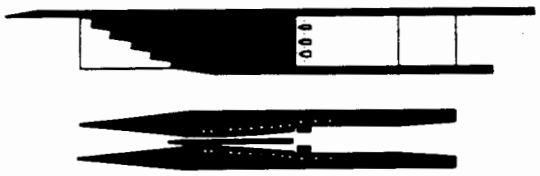

(e) NASA Langley step-strut engine.

Figure 2.- Scramjet engine design variations.

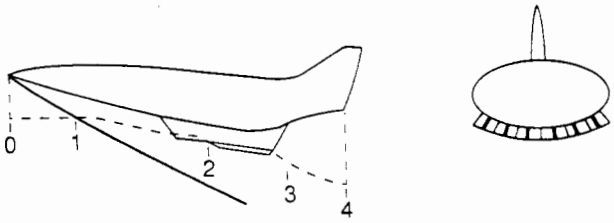

(a) Engine/airframe integration.

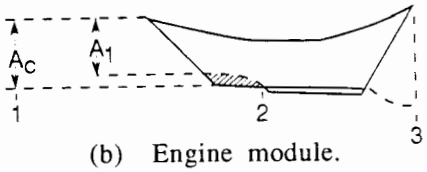

(b) Engine module.

Figure 3.- Sidewall compression scramjet.

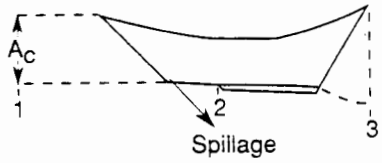

Figure 4.- Sidewall compression scramjet with alternate control volume.

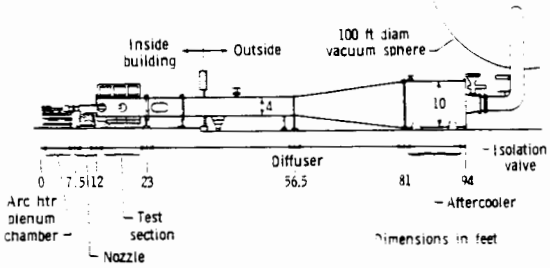

Figure 5.- Elevation view of the Arc-Heated Scramjet Test Facility.

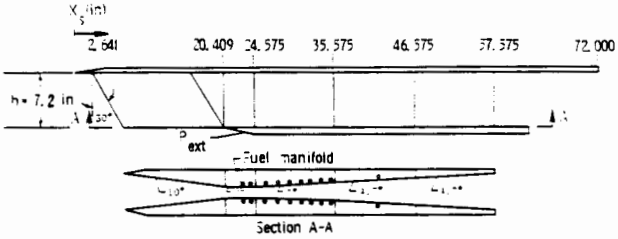

Figure 6.- Strutless parametric scramjet.

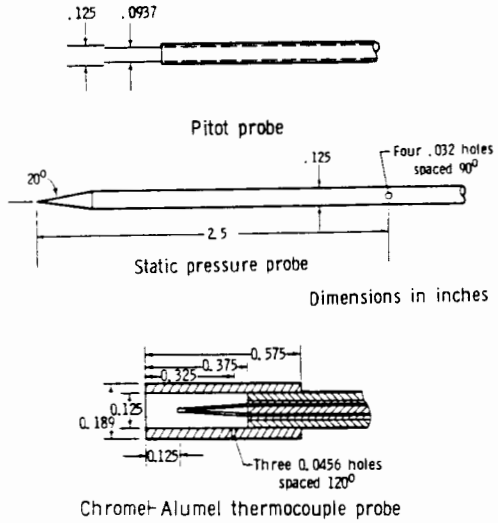

Figure 7.- Flow measurement probes.

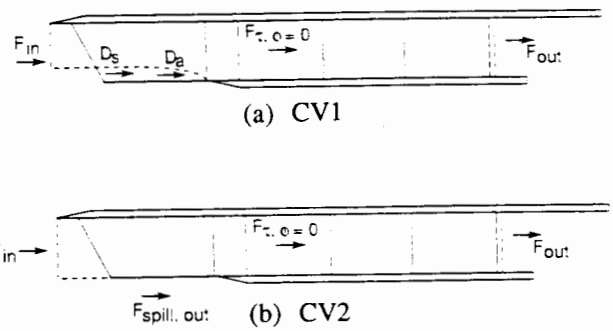

Figure 9.- Control volume definitions.

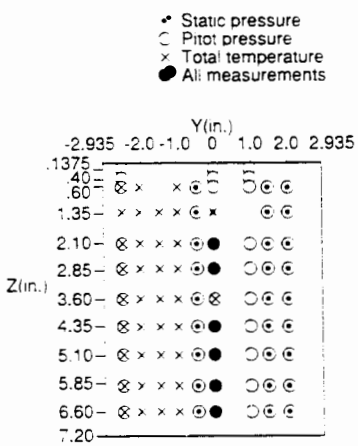

Figure 8.- Engine exit measurement locations.

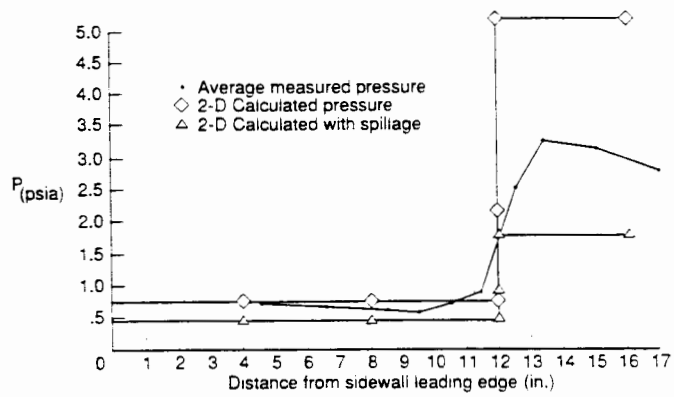

Figure 10.- Calculated and average inlet pressures.

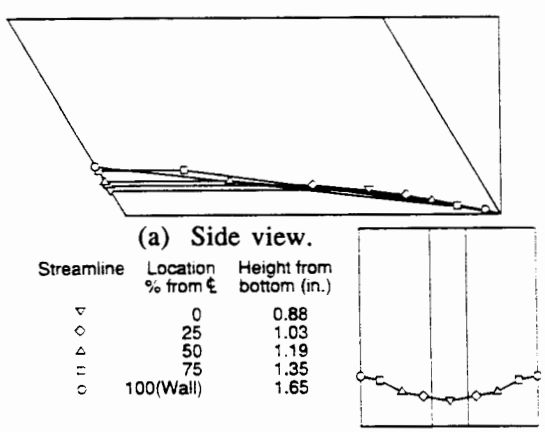

Figure 11.- Last captured streamlines.

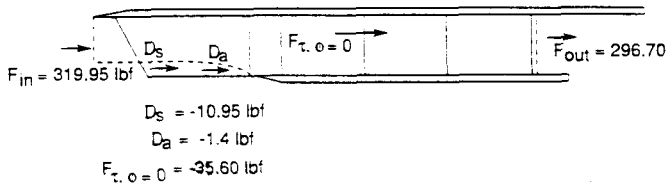

Figure 12.- Forces on CV1.

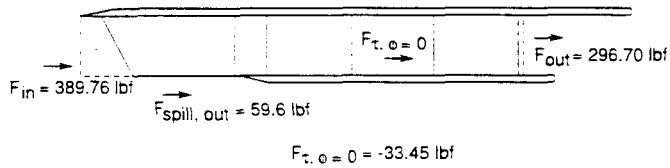

Figure 13.- Forces on CV2.